frontiers
in Remote Sensing

TYPE Original Research
PUBLISHED 11 March 2026
DOI 10.3389/frsen.2026.1751006

EDITED BY
Simona Niculescu,
Université de Bretagne Occidentale,
France

REVIEWED BY
Binbin Jiang,
Zhejiang University of Science and
Technology, China
Rania AlHossainy,
Benha University, Egypt

*CORRESPONDENCE
Ali Reza Payandeh,
✉ ali.reza.payandeh@jpl.nasa.gov

RECEIVED 21 November 2025
REVISED 14 February 2026
ACCEPTED 23 February 2026
PUBLISHED 11 March 2026

CITATION
Payandeh AR, Simard M, Jensen D, Campbell AD, van Deventer H and Christensen A (2026) A fully satellite-driven workflow for hydrodynamic modeling in data-scarce coastal systems: integrating ICESat-2, Sentinel-2, SWOT and reanalysis models. *Front. Remote Sens.* 7:1751006. doi: 10.3389/frsen.2026.1751006

A fully satellite-driven workflow for hydrodynamic modeling in data-scarce coastal systems: integrating ICESat-2, Sentinel-2, SWOT and reanalysis models

Ali Reza Payandeh[1]*, Marc Simard[1], Daniel Jensen[1], Anthony Daniel Campbell[2], Heidi van Deventer[3,4] and Alexandra Christensen[1]

[1]Jet Propulsion Laboratory, California Institute of Technology, Pasadena, CA, United States, [2]Goddard Earth Sciences Technology and Research, Greenbelt, MD, United States, [3]The Council for Scientific and Industrial Research, Pretoria, Gauteng, South Africa, [4]The University of Pretoria, Department of Geography, Geoinformatics and Meteorology, Pretoria, Gauteng, South Africa

Hydrodynamic models in coastal and estuarine systems are typically constrained by sparse bathymetry, boundary, and validation data, especially in regions where field campaigns are costly or impractical. Here we develop and test a fully satellite-driven framework for hydrodynamic modeling in South Africa's Langebaan Lagoon without using any local *in situ* measurements. Bathymetry is derived by training multispectral Sentinel-2 reflectance against ICESat-2 ATL24 photon-derived depths using an XGBoost model optimized with Bayesian search. The final satellite derived bathymetry reproduces independent ATL24 points with RMSE = 0.45 m and R^2 = 0.97. This bathymetry was used in a depth-averaged Delft3D Flexible Mesh model driven at the open boundary by TPXO tidal harmonics and by ERA5 winds. We validate modeled water surface elevation against 16 SWOT low-rate (250 m, unsmoothed) passes in 2023. SWOT−model comparisons yield an overall RMSE of 0.11 m and R^2 = 0.61, with typical point differences <0.10 m (~5% of the 2 m tidal range), and showed consistent spatial gradients in water level from the offshore boundary, through Saldanha Bay, and into the lagoon. At the offshore boundary, TPXO and SWOT sea surface heights agree closely (R^2 = 0.86). A ~26 min phase lag, determined using a lag-correlation analysis, reduces the TPXO−SWOT RMSE from 0.18 m to 0.11 m, indicating that phase differences explain some of the mismatch, with remaining differences likely linked to non-tidal signals. Our results demonstrate that combining passive optical, photon-counting LiDAR, radar interferometry, and global tidal/atmospheric models enables robust, transferrable hydrodynamic modeling in data-scarce coastal systems, offering a cost-effective pathway for monitoring.

KEYWORDS

bathymetry, Delft3D flexible mesh, hydrodynamic, ICESat-2, reanalysis models, Sentinel-2, SWOT, TPXO

1 Introduction

Coastal and estuarine systems are dynamic, largely driven by the constant motion of water. The meeting of tides, waves, and river inflows drives salinity gradients, sediment transport, and flooding and drying, which together shape water quality, habitat characteristics, function and distribution, as well as productivity of these environments. Understanding these dynamics is fundamental for predicting how ecosystems respond to change as human pressures and climate change impacts intensify. Such changes can include shifts in habitat distribution, salinity regimes, sediment transport pathways, carbon storage, sea level rise and eventually changes in wetland stability (Kirwan and Mudd, 2012; Kirwan and Megonigal, 2013; Spencer et al., 2016; Schuerch et al., 2018; Sorourian et al., 2020; Payandeh et al., 2019; Payandeh et al., 2021; Payandeh et al., 2022). A well-calibrated hydrodynamic model forms the foundation for simulating sediment movement, morphology, and even ecosystem responses to changes in water levels, salinity, and sediment dynamics (Brush and Harris, 2010; Ganju et al., 2016; Payandeh et al., 2025; Simard et al., 2026). Yet, the accuracy of such models depends strongly on the availability of reliable field data for bathymetry, boundary conditions, and validation. In practice, collecting these data in coastal wetlands, deltas, or estuaries is difficult. Field campaigns can be costly, constrained by permits and at the mercy of weather or access. Such challenges explain why many of the world's coastal environments remain only sparsely mapped and monitored (Båmstedt and Brugel, 2017; Mohseni et al., 2022; Vargas-Yáñez et al., 2025).

Recent advancements in satellite remote sensing and global reanalysis products now offer promising alternatives to traditional field-based monitoring, particularly in data-scarce and difficult to access coastal environments. High-resolution multispectral imagery from Sentinel-2 has enabled the routine estimation of bathymetry through aquatic optical remote sensing and wave kinematics techniques, with reported accuracies typically around Root Mean Square Error (RMSE) of ≤ 1.5 m and a mean absolute error of ~ 0.1–0.2 m in optically clear, non-turbid and shallow waters (e.g., Pacheco et al., 2015; Chénier et al., 2018; Traganos et al., 2018; Najar et al., 2022). Meanwhile, ICESat-2 laser altimetry has been shown to provide robust elevation "seed points" for calibrating passive satellite derived bathymetry workflows, enabling operational and spatially efficient bathymetric mapping (e.g., Babbel et al., 2021; Le et al., 2024; Corcoran et al., 2024; Jung et al., 2025). Complementing these remote observations are global tidal models such as TPXO, which assimilate satellite altimetry, with tidal elevation and current fields that are commonly used to force coastal model boundaries (e.g., Stammer et al., 2014; Yang et al., 2020). On the atmospheric side, the ERA5 reanalysis supplies hourly wind and pressure fields that have been shown to improve wave and surge simulations compared with earlier reanalysis products (Dullaart et al., 2020). Finally, the Surface Water and Ocean Topography (SWOT) mission provides two-dimensional maps of water surface elevation with sub-kilometer resolution over coastal oceans and estuaries, allowing direct comparison of model and SWOT measured water levels and improving calibration and validation of hydrodynamic models (Morrow et al., 2019; NASA/PO.DAAC, 2025). Together, these freely available datasets form a practical toolkit to initialize, force, and validate coastal hydrodynamic models reducing reliance on costly field campaigns while covering a larger area and longer time span than would otherwise be feasible.

However, a key gap remains: there is still no widely demonstrated, end-to-end workflow that can (i) derive bathymetry, (ii) prescribe open boundary tides and surface wind forcing, and (iii) calibrate/validate coastal hydrodynamics using only satellite and global products, without any local bathymetric surveys, tide gauges, or *in situ* meteorological measurements. This limits the transferability of remote sensing based modeling to truly data-scarce systems. Most existing applications of remote sensing driven hydrodynamic modeling still require some degree of *in situ* data for calibration or validation, such as tide gauge records, measured bathymetry, or meteorological observations to, for example, supply tide gauge time series for calibration and verification, initialize seed depths for satellite derived bathymetry, or provide wind forcing inputs (Babbel et al., 2021; Williams and Esteves, 2017). This dependency limits their transferability to truly data-scarce regions, where logistical constraints or resource limitations prevent sustained ground-based monitoring (Ashphaq et al., 2021; Williams and Esteves, 2017).

In sub-Saharan and South African contexts, estuarine and lagoon systems are frequently characterized as data limited, and recent syntheses highlight both the ecological importance of these systems and the relative scarcity of long-term observational records needed for modeling and management (Van Niekerk et al., 2022; Whitfield et al., 2012). Langebaan Lagoon (Figure 1) is one such system: a shallow, microtidal lagoon of high conservation value, protected within South Africa's West Coast National Park and designated as a Ramsar site (Hanekom et al., 2009). Coastal lagoons are estimated to occur along only 13% of the extent of the world's coastlines, and most extensively along 18% of the African coastline (Badcock and Barnes, 1981). Lagoons form important breeding and nursery habitats for fin and shellfish, serving poor communities with food (Miththapala, 2013). Anthropogenic impacts, such as coastal development and industry, as well as increasing temperatures and evapotranspiration associated with climate change, can negatively impact the function of these systems through increased sedimentation (Essel et al., 2019), rendering coastal lagoons vulnerable. These pressures are acutely relevant in the coupled Saldanha Bay–Langebaan Lagoon system. The development of, and continuous dredging operations at, the Saldanha Bay port, together with ongoing and increasing residential development along the coast (Krug, 1999; Du Toit et al., 2022), have raised concerns about the hydrodynamics and sedimentation in the bay that is shared with the Langebaan Lagoon mouth. Changes in bathymetry between 1957 and 1977 showed accumulation of sediments at the Langebaan Lagoon mouth, whereas erosion occurred in other parts of the bay (Henrico and Bezuidenhout, 2020). Continuous monitoring of the bathymetry of both the bay and the Langebaan Lagoon, to better characterise possible natural inter- and intra-annual variations relative to those resulting from anthropogenic events and their impacts on ecosystems and species, is highly recommended. Against this backdrop, Langebaan Lagoon is an ideal testbed for examining whether a fully satellite-driven modeling workflow can be used where conventional observations are sparse or absent.

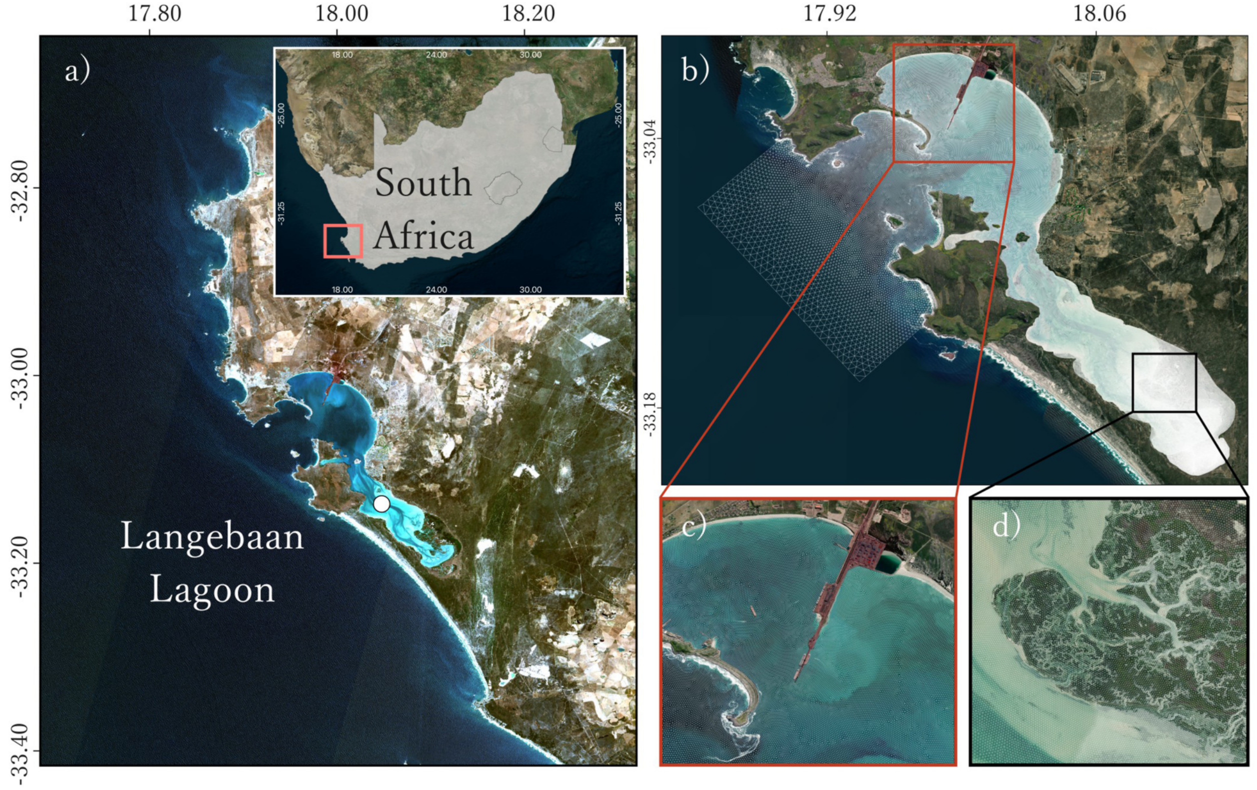

FIGURE 1
Spatial context and computational mesh. **(a)** The location of Langebaan Lagoon on the western margin of South Africa, highlighted within the red box. **(b–d)** The Delft3D Flexible Mesh grid applied in this study.

To overcome the limitations of conventional approaches, this study develops a fully satellite driven, end-to-end framework for hydrodynamic modeling in coastal lagoons where field data are limited or unavailable. The workflow combines satellite-derived bathymetry, generated through a machine-learning approach using ICESat-2 and Sentinel-2 data, with a two-dimensional Delft3D Flexible Mesh model forced by global tidal and atmospheric reanalysis products. Model calibration and validation are carried out using spaceborne sea surface height observations, eliminating the need for local gauges or survey campaigns. By applying this framework to South Africa's Langebaan Lagoon, we demonstrate its capability to reproduce key hydrodynamic processes in a microtidal, data scarce environment. The objectives are to (1) evaluate the feasibility of generating reliable bathymetry without *in situ* depth measurements, and (2) to assess the performance of a hydrodynamic model initialized, forced, and validated entirely from spaceborne and global products. While this study focuses on a single test case, the workflow is general and could be transferred to other coastal systems, especially where access, safety, or cost makes field measurements impractical.

2 Methods

2.1 Bathymetry estimation

Bathymetry was estimated by training multispectral surface reflectance from Sentinel-2 with photon-derived elevations from ICESat-2 ATL24 products (Parrish et al., 2025). The ATL24 product provides along-track bathymetric retrievals (referenced to EGM08) by detecting photons that penetrate the water column and return from the seabed. These elevations are derived from ICESat-2 L2A Global Geolocated Photon Data (ATL03) and are already refraction corrected. Figure 2 shows two examples of ATL24 tracks across the lagoon. Depths along the track show intertidal and subtidal flats, with tidal channels clearly resolved. Deeper tidal channels appear as darker green meandering features in Sentinel-2 imagery, and reach depths of up to −8 m (referenced to EGM08), while brighter sandy lagoon floors in intertidal and subtidal areas correspond to shallower depths between −3 and −1 m. In total, 17 ICESat-2 tracks were used in this study. Most crossed the lagoon itself, while several extended into Saldanha Bay and the adjacent offshore area. Figure 3 shows the location of all ICESAT-2 ground tracks that were used to train the model.

Sentinel-2 provides multispectral imagery at 10–20 m spatial resolution, which captures optical variations in the water column that can be related to depth. Sentinel-2 imagery allowed us to train a predictive model capable of extending point-based ICESat-2 depths across the full lagoon and bay. For model training, we focused on bands and ratios that have been shown to correlate well with bathymetry (Casal et al., 2019; Caballero and Stumpf, 2020; Wei et al., 2020). Specifically, we used the blue, green and red band ratios, the Normalized Difference Water Index (NDWI), and individual reflectance values from the red-edge bands (Table 1). These predictors provide a balance between the sensitivity to water

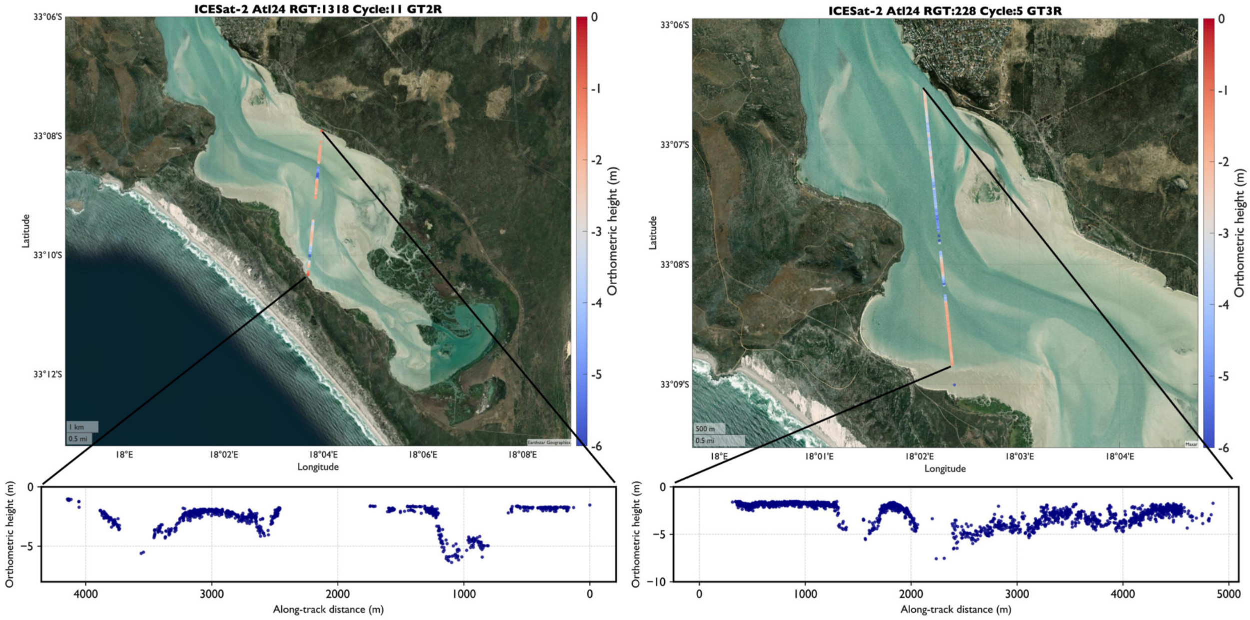

FIGURE 2
Examples of ICESat-2 ATL24 bathymetry elevations (referenced to EGM08). Each panel is labeled with the corresponding Reference Ground Track (RGT) number, cycle number, and laser beam identifier.

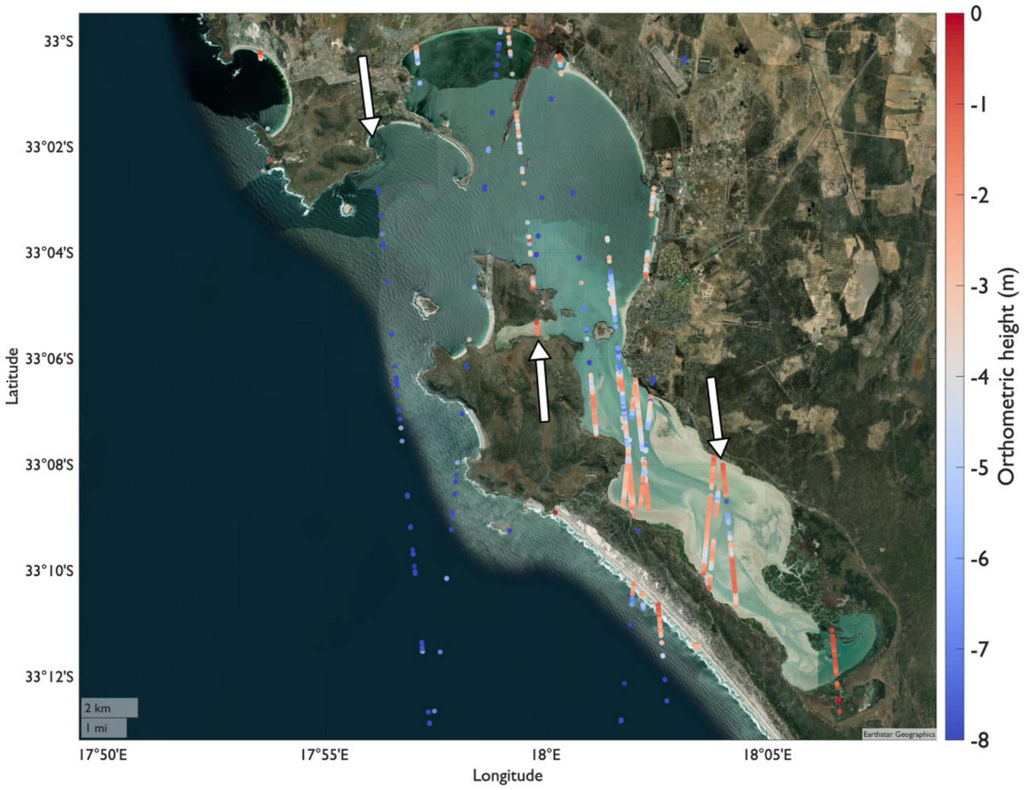

FIGURE 3
All ICESat-2 ATL24 bathymetry tracks (referenced to EGM08) used in this study to drive bathymetry. Tracks indicated by arrows (~20% of all points) were reserved for validation, while the remaining tracks were used for model training.

TABLE 1 Sentinel-2 predictors used to derive bathymetry. Band designations and central wavelengths are from the Sentinel-2 MSI sensor specifications.

Predictor	Description	Central wavelength (nm)
B2/B3	Ratio of blue to green	490/560
B2/B4	Ratio of blue to red	490/665
B3/B8	Ratio of green to NIR	560/842
B4/B8	Ratio of red to NIR	665/842
NDWI	Normalized difference water index	(Green–NIR)/(Green + NIR)
B5	Red-edge 1	705
B6	Red-edge 2	740
B7	Red-edge 3	783

depth and reduced influence of atmospheric and surface effects. Sentinel-2 imagery from both Sentinel-2A and Sentinel-2B platforms were used. All predictors were computed after ACOLITE resampling, therefore no additional band co-registration correction was applied. Sentinel-2 images were processed using the ACOLITE application (version 20250402.0) to correct for atmospheric effects and remove sun glint (Vanhellemont and Ruddick, 2016). ACOLITE adopts the Dark Spectrum Fitting (DSF) atmospheric correction with integrated sun-glint correction (Vanhellemont and Ruddick, 2018; Vanhellemont, 2019; Vanhellemont, 2020). DSF estimates atmospheric path reflectance directly from the low-reflectance tail of the image radiance distribution, without requiring pre-defined dark pixels. It has been shown to perform robustly in a wide range of coastal and optically complex waters, including clear and moderately turbid waters (e.g., Page et al., 2019; Wang et al., 2019; Ciancia et al., 2020), as well as complex coastal and estuarine waters (e.g., Balasubramanian et al., 2020; Caballero et al., 2020). In our case, the full Sentinel-2 tile includes both bright, sand dominated shallow areas inside the lagoon and darker waters in the deeper channels, Saldanha Bay, and the adjacent offshore region. These darker water pixels provide the dark spectrum needed to constrain path reflectance, while the method adapts to spatial variability in turbidity and bottom type across the scene (Vanhellemont, 2019; Vanhellemont, 2020; Wang et al., 2021). Sun glint was corrected using ACOLITE's shortwave infrared (SWIR)–based glint estimation option, which derives the glint signal from SWIR bands (for Sentinel-2: B11/B12) following the approach of Harmel et al. (2018). This correction is applied after DSF atmospheric correction and is documented in Vanhellemont (2019).

To illustrate the effect of the atmospheric and glint correction, Supplementary Figure S1 shows two representative Sentinel-2 scenes before (top of atmosphere) and after correction (surface reflectance). The corrected image shows reduced haze and glint, clearer separation between land and water, and enhanced expression of underwater features. We did not have *in situ* above water spectra or AERONET-OC data in the Langebaan Lagoon, so atmospheric correction accuracy was assessed indirectly. First, we visually inspected DSF corrected reflectance for multiple dates, confirming stable spectral shapes and magnitudes in invariant deep water areas and the expected blue–green dominance in clearer lagoon water, consistent with previous DSF validation studies in coastal waters. Second, the subsequent bathymetry retrievals showed consistent performance across 16 independent Sentinel-2 scenes (Table 2), suggesting that any residual atmospheric artifacts did not dominate the depth–reflectance relationship used for deriving bathymetry.

TABLE 2 Bathymetry validation for each Sentinel-2 image using the XGBoost model optimized with Bayesian search. Modeled depths are compared against independent ATL24 validation points.

Image	RMSE (m)	R^2
Image 1	0.45	0.97
Image 2	0.47	0.97
Image 3	0.44	0.97
Image 4	0.42	0.97
Image 5	0.54	0.96
Image 6	0.43	0.97
Image 7	0.41	0.97
Image 8	0.44	0.97
Image 9	0.45	0.97
Image 10	0.46	0.97
Image 11	0.49	0.96
Image 12	0.47	0.97
Image 13	0.36	0.98
Image 14	0.55	0.95
Image 15	0.57	0.95
Image 16	0.42	0.97
Average	**0.46**	**0.97**

ICESat-2 ATL24 points were filtered based on quality flags and clarity indicators. Only photons classified as bathymetric bottom returns (class_ph = 40) with confidence values greater than 0.8 were retained. Additional depth and along-track filters were applied on a per-track basis to remove misclassified surface returns and noisy edge segments, guided by visual inspection of photon elevation profiles. These combined criteria reduced false bathymetric

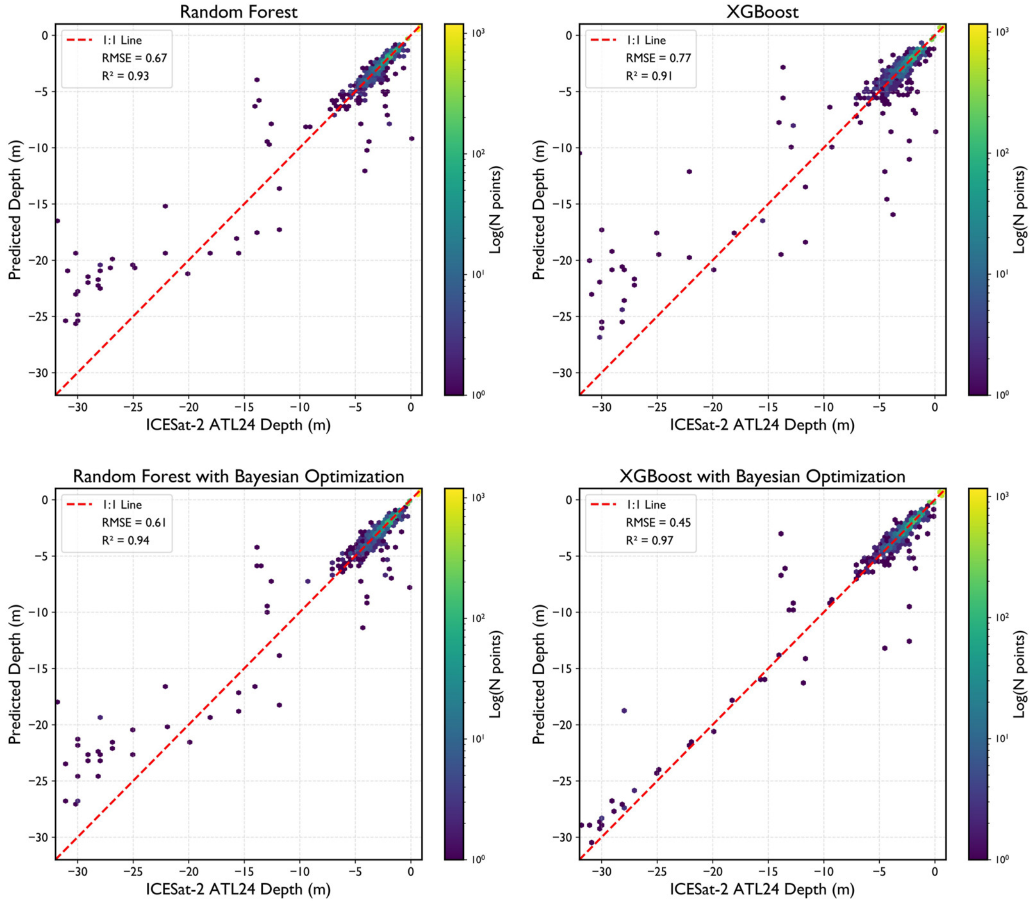

FIGURE 4
Comparison of model performance for bathymetry prediction using different machine learning approaches: Random Forest, Random Forest with Bayesian optimization, XGBoost, and XGBoost with Bayesian optimization. Performance was evaluated on an independent validation set, showing that XGBoost with Bayesian optimization achieved the best performance.

detections while preserving continuous bottom profiles across lagoon, bay, and offshore environments. ATL24 points then co-located with Sentinel-2 pixels to match reflectance and depth values. This produced a paired dataset of depth and reflectance values, which formed the input for model training. ATL24 bathymetry points were divided into independent training and validation sets using ICESat-2 track as the grouping variable: approximately 80% of ATL24 points (14 tracks) were used for training and the remaining 20% (3 tracks) were reserved for validation. Entire tracks were assigned either to the training or validation set, reducing spatial autocorrelation between training and validation samples and ensuring an unbiased evaluation. The validation tracks were selected to span the full range of environmental settings in the study area, one in deep offshore waters, one within the bay, and one in the shallow lagoon (Figure 3).

Several machine learning models were tested to predict bathymetry from reflectance, including Random Forest, Random Forest with Bayesian optimization, XGBoost, and XGBoost with Bayesian optimization. For the models without Bayesian optimization, the hyperparameters were adjusted manually based on iterative trial-and-error rather than through an automated search. In the Random Forest models, the number of trees, maximum tree depth, and the minimum number of samples required to split a node were varied. In the XGBoost models, different combinations of learning rate, maximum tree depth, and subsampling ratio were tested. Bayesian optimization was then applied to both models to automatically search for the best parameters. For the XGBoost Bayesian optimization, the search space included learning rate (0.01–0.3), maximum tree depth (3–12), subsample ratio (0.5–1.0), column sampling ratio (0.5–1.0), and number of estimators (100–1,000). The optimization objective was minimization of validation RMSE. Performance was evaluated using the validation set. Reflectance from the first Sentinel-2 image was used to select the best-performing machine learning model (Figure 4). Once the optimal model was identified, it was applied to the remaining 15 Sentinel-2 scenes to generate additional depth estimates. Bathymetry derived from each of these scenes was then validated independently against ATL24 points.

Among all models, XGBoost with Bayesian optimization showed the best performance with an RMSE of 0.45 m and R^2 of 0.97 relative to ICESat-2 ATL24 photon derived depths, and was therefore selected as the final model to derive bathymetry (Figure 4). Validation of the individual bathymetries demonstrated that the

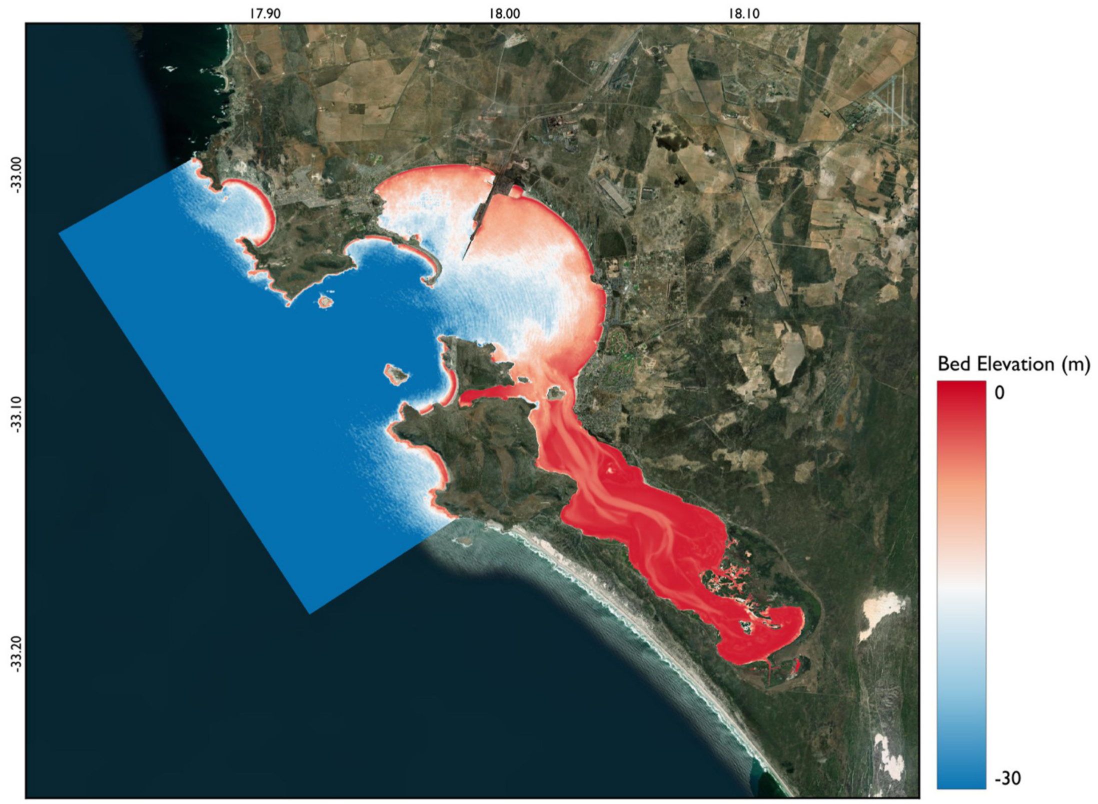

FIGURE 5
Final satellite-derived bathymetry for Langebaan Lagoon and Saldanha Bay. Depths represent the averaged prediction from 16 cloud-free Sentinel-2 scenes after training on ICESat-2 ATL24 points.

model remained consistently accurate across scenes with varying wave conditions, supporting the robustness of the final averaged product (Table 2). Across these 16 images, validation RMSE values ranged from 0.36 to 0.57 m, with corresponding R^2 values between 0.95 and 0.98, and an overall average RMSE of 0.46 m and R^2 of 0.97.

During model development, a recurring challenge was interference from surface waves, which introduced noise into the predicted bathymetry. Band ratios helped to reduce these effects, but to further minimize wave-related interference, the resulting depth maps from all 16 images were averaged to reduce wave-related noise and produce the final bathymetry product. Finally, a Gaussian filter was applied to the averaged bathymetry grid to further suppress high-frequency noise and improve the spatial continuity of depth estimates. We used a small kernel ($\sigma \approx 1$ pixel; 3× three window) to reduce residual wave/speckle artifacts while preserving tidal channel gradients and other bathymetric features at lagoon scales. The final processed bathymetry is shown in Figure 5.

2.2 Hydrodynamic model setup

A two-dimensional, depth-averaged hydrodynamic model of Langebaan Lagoon was developed using the Delft3D Flexible Mesh Suite (Delft3D FM). Delft3D FM is a finite volume modeling system that solves the unsteady, nonlinear shallow water equations on an unstructured grid, making it well suited for estuarine and coastal environments with irregular geometries and complex bathymetry (Deltares, 2021). Unlike structured grids, the unstructured approach allows flexible refinement in areas of interest while maintaining efficiency in less dynamic regions. The unstructured grid was developed using Aquaveo's Surface Water Modeling System (SMS) (Zundel, 2000). Mesh resolution was intentionally varied to capture landscape complexity while maintaining computational efficiency. Higher-resolution triangular elements (~10 m) were applied within the lagoon's tidal channels, intertidal flats, and constricted inlets to ensure accurate representation of flow pathways. Coarser elements (40–200 m) were used in Saldanha Bay and offshore areas, where topographic complexity is lower. This gradation balanced model accuracy with computational efficiency. Islands were removed from the computational mesh. Prior to simulation, the mesh was evaluated for smoothness, orthogonality, and related quality metrics to meet accepted numerical standards. Specifically, the mesh achieved orthogonality < 0.01 and smoothness of 1.08 on average with a maximum of 1.2. These values fall within commonly recommended stability ranges for coastal hydrodynamic modeling, and no problematic elements were identified in the lagoon or boundary regions. The final mesh comprised 171,182 nodes and 339,119 elements (Figure 1).

Open boundary conditions were imposed along the offshore edge of the domain using tidal amplitudes and phases taken from the TPXO global tidal model (Egbert and Erofeeva, 2002). As an additional check, we later compared TPXO reconstructed water

TABLE 3 **Tidal harmonic constituents used to force the offshore boundary. Amplitudes (m) and phases (degrees) were taken from TPXO.**

Constituent	Amplitude (m)	Phase (deg)
M2	0.506	34.0
S2	0.218	52.7
N2	0.109	26.9
K2	0.063	50.1
K1	0.055	105.6
SA	0.032	328.0
MU2	0.018	5.1
O1	0.016	234.9
NU2	0.016	31.8
2N2	0.016	15.5
P1	0.015	109.3
L2	0.013	25.9

levels against SWOT observations at the offshore boundary and found that they generally agreed well, which increases confidence in using TPXO as the tidal driver (Section 4.2). Twelve dominant tidal constituents were extracted from TPXO and applied to the eastern offshore boundary. Nodal corrections in Delft3d FM were set to be updated and applied to the tidal constituents every 24 h. The tidal signal in the study area is predominantly semidiurnal, with M2 being the largest driver, followed by S2 and N2. Their amplitudes are 0.50 m, 0.21 m and 0.10 m, respectively, indicating a clear semidiurnal dominance with smaller diurnal modulation from constituents such as K1 and O1 and P1. The full list of constituents, amplitudes and phases used at the boundary is given in Table 3. In addition to prescribing tidal forcing along the eastern offshore boundary, Neumann (free outflow) conditions were applied at the northern and southern offshore boundaries to allow unrestricted water exchange. Hourly wind forcing was taken from the ERA5 reanalysis and applied to the model as surface forcing. Wind stress was calculated in the model using the drag coefficient formula of Large and Pond (1981), and the resulting stresses were applied as surface momentum fluxes in Delft3D-FM. ERA5 was chosen for its hourly temporal resolution, global coverage, and a horizontal grid spacing of 0.25°, which provides consistent, gap-free atmospheric fields appropriate for forcing models in data-scarce regions (Hersbach et al., 2020).

2.3 SWOT data processing

To evaluate model performance, we made use of observations from the NASA SWOT mission. SWOT carries the Ka-band Radar Interferometer (KaRIn), which provides wide swath measurements of water surface heights over both the ocean and inland water bodies. The mission produces two main data streams tailored for different science communities: a high-rate (HR) stream for rivers and lakes, and a low-rate (LR) stream designed primarily for oceanography. Ideally, the HR products would have been the best fit for a semi-enclosed coastal system like Langebaan Lagoon, because of their finer resolution and suitability for smaller water bodies. However, HR data are only downlinked to selected target areas and no HR coverage was available for Langebaan Lagoon during the study period. For this reason, we relied on the LR products, specifically the Level-2 (L2) LR Sea Surface Height (SSH) data, which are available globally every 21 days, including over coastal zones.

The SWOT processing workflow is shown in Figure 6. Sixteen SWOT pass acquisitions intersecting the Langebaan Lagoon domain were downloaded from the PO.DAAC archive and processed (Christensen, 2025). For each pass we used the SWOT Level-2 Low Rate SSH Expert (SWOT_L2_LR_SSH_Expert_2.0) and Unsmoothed (SWOT_L2_LR_SSH_Unsmoothed_2.0) products (version C). The Expert file, provided on a 2 km swath-aligned grid with correction fields and diagnostic metadata, and the Unsmoothed file, which contains the native KaRIn measurements at roughly 250 m sampling and about 500 m resolution. Our final comparisons with the hydrodynamic model relied solely on the Unsmoothed SSH at approximately 250 m resolution, as this dataset preserves the finer spatial variability needed for lagoon-scale evaluation.

The expert files provide crossover correction heights. The crossover correction removes large-scale swath biases inferred from differences at pass intersections where ascending and descending SWOT swaths overlap (crossover points). Because this correction is provided on the 2-km Expert grid, we used piecewise linear interpolation to transfer the correction heights to the native 250-m (unsmoothed) pixels. We then computed water surface elevation for every valid Unsmoothed point using a geoid derived from a GTX file (EGM08). Geoid heights were interpolated from NOAA VDatum GTX grid points (NOAA National Ocean Service, 2025) to the SWOT Unsmoothed 250-m grid. These geoid values were then subtracted from the KaRIn SSH, after applying the crossover corrections, to produce the water surface elevation (WSE) used in model comparisons. For clarity, Equation 1 describes the WSE computed from the Unsmoothed L2 product (NASA/PO.DAAC, 2025):

$$\mathrm{WSE} = ssh_{\mathrm{karin\_2}} + height\_cor\_xover - geoid_{\mathrm{GTX}} \tag{1}$$

Where ssh_karin_2 is the Unsmoothed KaRIn SSH field, height_cor_xover is the crossover correction interpolated from the matching Expert file, and geoidGTX is the external geoid height sampled from the GTX grid (referenced to EGM08). After computing WSE for each pass, we applied a set of quality control steps. First, we used the interferometric total coherence as the primary quality flag and retained only pixels with coherence ≥ 0.8. Coherence provides a direct measure of phase stability between the two KaRIn antennas, so low-coherence pixels are more likely to be noise dominated and yield unreliable heights. In addition, we masked land and near coast pixels where SWOT retrievals are known to be less reliable, and discarded extreme outliers. The cleaned Unsmoothed WSE fields were saved as NetCDF outputs for each pass, and these per-pass Unsmoothed products (16 in total for 2023) formed the observational dataset used in model comparisons.

We also examined the auxiliary tidal correction fields provided in the SWOT L2 Expert product, including the solid Earth tide, load tide, and pole tide terms. Across all passes and within the Langebaan

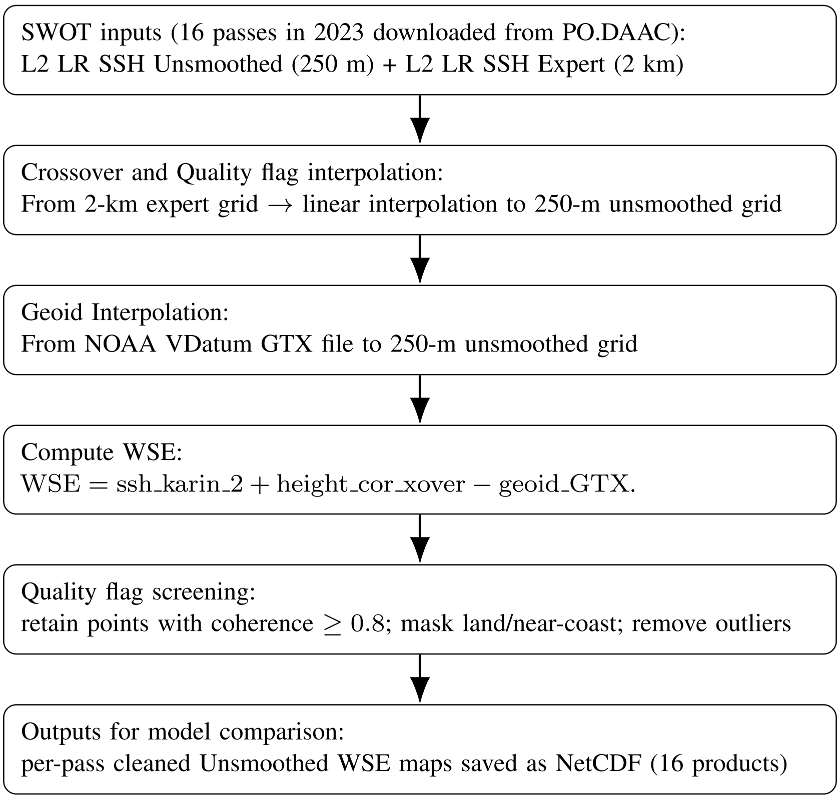

FIGURE 6
SWOT L2 LR processing workflow used to generate geoid-referenced 250-m water surface elevation (WSE) maps for model evaluation.

Lagoon domain, these corrections were consistently small, with magnitudes on the order of 10^{-3} m. This is several orders of magnitude smaller than the tidal range in the area (~ 2 m), so their contribution to the total water surface elevation is negligible.

3 Hydrodynamic model performance

To evaluate model performance, we compared modeled water surface elevation with SWOT observations for 16 passes over Langebaan Lagoon during the 2023 simulation period. For each pass, we interpolated the model results from the unstructured mesh onto the corresponding SWOT grid coordinates so that the comparison was spatially consistent. This made it straightforward to compare maps, time snapshots, and point by point statistics. Our sensitivity tests showed that the model was most sensitive to bottom roughness. We used the Chézy friction formulation (Chézy, 1775) and tuned the Chézy coefficient by iterating model runs and comparing to SWOT. After trying a range of values we found that a Chézy coefficient of 57 $m^{1/2}/s$ produced the best overall agreement with all the SWOT observations, so that value was used in the final simulations (Table 4).

Figure 7 shows three example comparisons between model and SWOT for different acquisition dates. For the September 1 overpass, the spatial pattern was consistent between the model and SWOT. Water levels in the offshore area were about −0.2 to −0.4 m and the southeast end of the lagoon fell to roughly −0.9 m in both datasets.

TABLE 4 **Sensitivity of model performance to the Chézy friction coefficient. Performance metrics are computed from collocated SWOT–model water surface elevations.**

Chézy ($m^{1/2}/s$)	RMSE (m)	R^2
45	0.19	0.47
50	0.15	0.54
57	0.11	0.61
65	0.14	0.58
75	0.18	0.49

On November 24 the bay showed higher water levels, roughly 0.3–0.4 m in Saldanha Bay, with lower values near the southeast lagoon around −0.1 m. SWOT reported slightly higher elevations in the bay, up to 0.5 m, whereas the model peaked near 0.3 m. For the December 15 pass, the model showed water levels of about −0.3 to −0.2 m in the bay and higher values toward the southeast lagoon near 0 m. SWOT captured the same pattern but with slightly higher values in the lagoon, up to about 0.1 m. We also show scatter plots for these three passes and computed standard metrics to quantify agreement. The RMSEs were 0.07 m, 0.07 m and 0.05 m, and the corresponding R-squared values were 0.64, 0.53 and 0.54 for September 1, November 24 and December 15, respectively. To summarize performance across all SWOT acquisitions, Table 5 reports per-pass validation statistics for all 16 passes. Taken

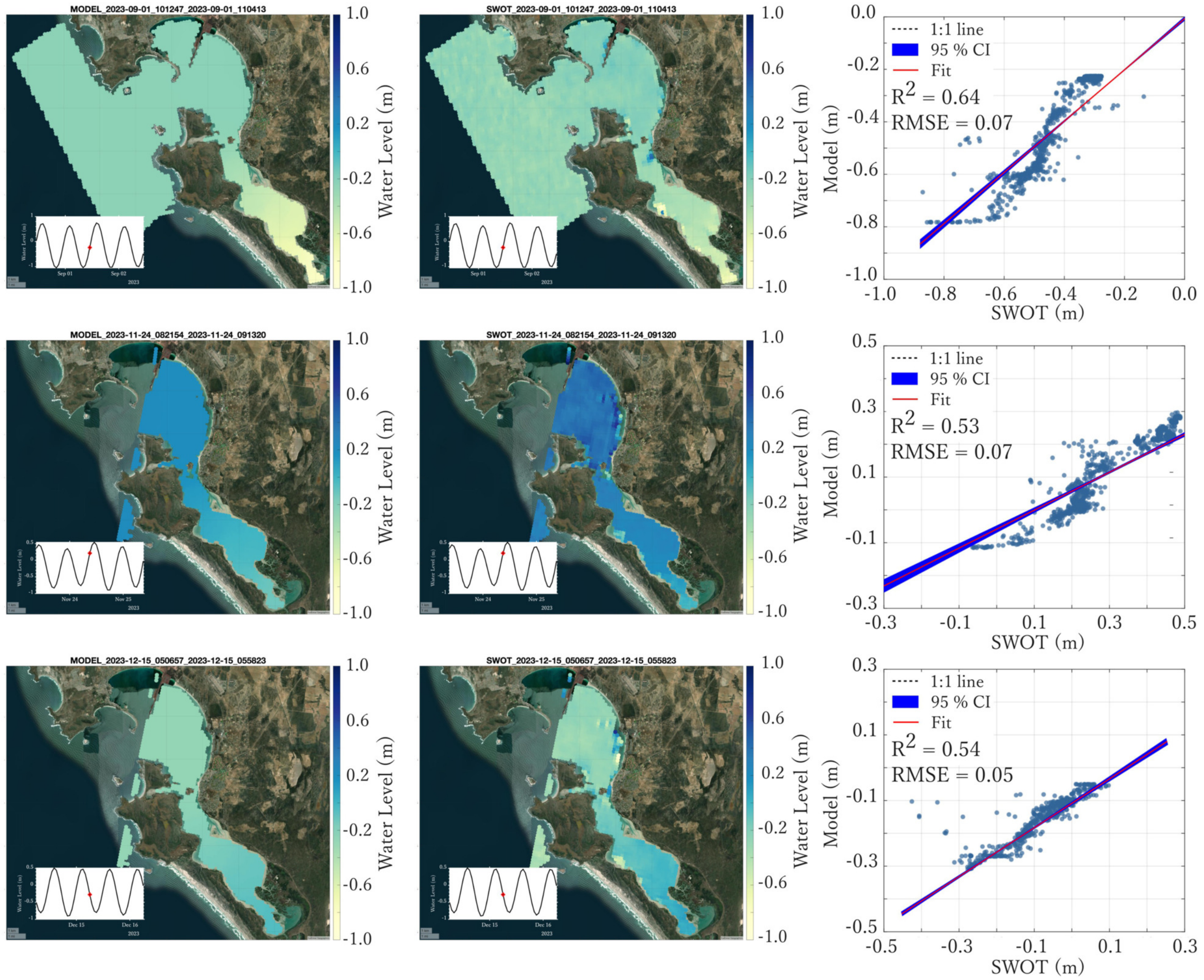

FIGURE 7
Comparison of modeled water surface elevation and SWOT observations for three acquisitions over Langebaan Lagoon. Maps show spatial patterns from the model (left) and SWOT (center), with corresponding scatter plots (right). Results are shown for September 1, November 24, and 15 December 2023 passes. Scatter plots include regression fits and performance metrics (RMSE and R^2).

together, these results indicate that the model reproduces the main spatial patterns and timing seen by SWOT and performs well for lagoon-scale validation. Figure 8 shows the scatter plot of collocated model *versus* SWOT water surface elevations for all 16 passes. The scatter showed a clear relationship between the two datasets. The overall statistics were $R^2 = 0.61$ and RMSE = 0.11 m across all passes. The model explained most of the observed variance in the offshore area, inside the bay and at the lagoon. Typical average point differences were of the order of less than 10 cm, which was small (~5%) relative to the system tidal range (~2 m).

4 Discussion

4.1 Bathymetry uncertainties

Bathymetry derived from ICESat-2 ATL24 and Sentinel-2 inevitably has non-negligible uncertainty. Early validation studies of ICESat-2 bathymetry showed typical errors on the order of a few tenths of a centimeter to about a meter depending on return quality and local conditions (Parrish et al., 2019; Parrish et al., 2025), so ATL24 cannot be treated as a perfect ground truth set at this location. Machine-learning approaches that combine ATL24 seed points with Sentinel-2 reflectance have proven effective at extending along-track depths into full maps, and recent studies reported satellite derived bathymetry errors typically in the 1 m ± 0.5 m range for comparable coastal environments, with a few examples reaching lower RMSEs when seed points were abundant and water clarity was high (Xu et al., 2023). In the case of the Langebaan Lagoon's analysis, the XGBoost model tuned with Bayesian optimization reproduced ATL24 itself with RMSE = 0.45 m and $R^2 = 0.97$, which is comparable but must be interpreted carefully: that error is relative to ATL24, not to independent sonar or Light Detection and Radar (LiDAR) surveys.

Depths in the Langebaan Lagoon ranges from near 1 m on tidal flats to about 40 m offshore according to regional charts and local studies of Saldanha Bay (Du Toit et al., 2022), so a fixed vertical error of a few decimeters has very different meaning across the lagoon. It

TABLE 5 **Per-pass validation statistics comparing modeled and SWOT LR Unsmoothed WSE.**

Cycle-pass	Date (UTC)	RMSE (m)	R^2
002–014	2023-08-11	0.12	0.58
002–027	2023-08-12	0.10	0.63
003–014	2023-09-01	0.07	0.64
003–027	2023-09-01	0.09	0.60
005–014	2023-10-13	0.13	0.56
005–027	2023-10-13	0.11	0.59
006–014	2023-11-03	0.12	0.57
006–027	2023-11-03	0.14	0.52
007–014	2023-11-23	0.08	0.62
007–014	2023-11-23	0.10	0.60
007–027	2023-11-24	0.07	0.53
007–027	2023-11-24	0.09	0.55
008–014	2023-12-14	0.16	0.49
008–014	2023-12-14	0.15	0.50
008–027	2023-12-15	0.05	0.54
008–027	2023-12-15	0.06	0.56
All passes	–	0.11	0.61

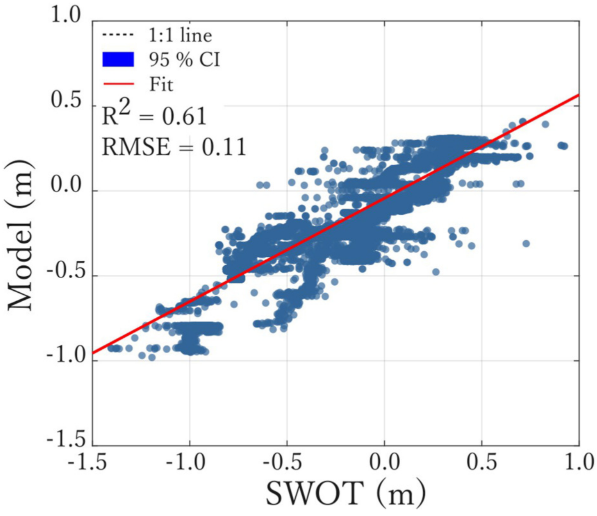

FIGURE 8
Scatter plot of collocated model *versus* SWOT water surface elevations for all 16 passes.

is negligible in deep channels but potentially large relative to intertidal flats and shallow channels, where a 0.45 m error is a large fraction of depth. In addition, optical limits and turbidity remain a hard constraint: Sentinel-2-based bathymetry loses sensitivity as water clarity decreases and as depths approach the optical penetration limit, and several evaluation studies have shown rapidly increasing errors in turbid or deep zones (e.g., Wei et al., 2024). Therefore, our deeper offshore (~35–40 m) areas are at the edge of optical penetration, while shallow lagoon (<8 m) zones are more reliably measured. Even in clear water, passive optical satellite derived bathymetry has a finite penetration depth set by exponential light attenuation; beyond roughly ~20–30 m (often shallower in non-oligotrophic conditions), the depth–reflectance relationship weakens and predictions tend to saturate, leading to rapidly increasing uncertainty with depth (Forfinski-Sarkozi and Parrish, 2016; Jasinski et al., 2016; Parrish et al., 2019; Xu et al., 2023; Caballero and Stumpf, 2020). Accordingly, we treat the offshore bathymetry (> 20 m) with higher-uncertainty than the lagoon interior, where depths are mostly < 8 m and optical sensitivity is stronger. However, in very shallow water ICESat-2 itself can underestimate depth when surface and bottom signals blur. This is a known limitation of photon-counting bathymetry in very shallow water, where wave state, water clarity, and limited separation between surface and bottom returns can increase misclassification risk and vertical uncertainty. ATL24 therefore provides per-point confidence/uncertainty metadata which we used to filter out points with high uncertainty (Parrish et al., 2019; 2025).

Uncertainty in the bathymetry translates directly into uncertainty in the hydrodynamic simulations. The modeling literature shows repeatedly that tidal amplitudes, phase propagation, local current speeds and inundation footprints are all sensitive to bathymetric detail; even modest vertical errors or smoothed small-scale features can change flow convergence, dissipation, and the local tidal prism (Cea and French, 2012). In our simulations, a 0.4–0.5 m typical bathymetry error (relative to ATL24) was small compared to the 30–40 m offshore depths but could produce sizeable relative changes in the shallow channels and flats where frictional effects matter most. Practically, this meant that some of the scatter against SWOT inside the lagoon could be traced to local depth mismatches rather than to fundamental failings of the hydrodynamic solver. It also explained why bottom friction tuning (the Chézy coefficient) had a strong leverage on fit metrics, i.e., calibration partly compensated for residual depth errors.

4.2 Boundary condition uncertainties

Global harmonic solutions such as TPXO are practical and easy to use as open boundary conditions because they give amplitudes and phases for the main tidal constituents everywhere and are widely validated against altimetry and tide gauges (Egbert and Erofeeva, 2002; Stammer et al., 2014). At the same time, several studies have shown that global models lose accuracy close to complex coastlines and in shallow, semi-enclosed seas where local bathymetry and resonance effects matter (Stammer et al., 2014; Zaron and Elipot, 2020; Gregg et al., 2024). Typical errors reported in regional evaluations are on the order of a few to a few tens of centimeters for the dominant constituents, although the exact value depends on local geometry and the quality of coastal bathymetry used in the global inversion (Stammer et al., 2014; Zaron and Elipot, 2020).

In this study, the model open boundary was forced with TPXO tidal harmonics. That makes it important to check how TPXO and SWOT agreed at the offshore boundary, because the boundary, located about 7 km seaward of the bay mouth and about 17 km from the lagoon mouth, so the boundary was reasonably close to the region of interest

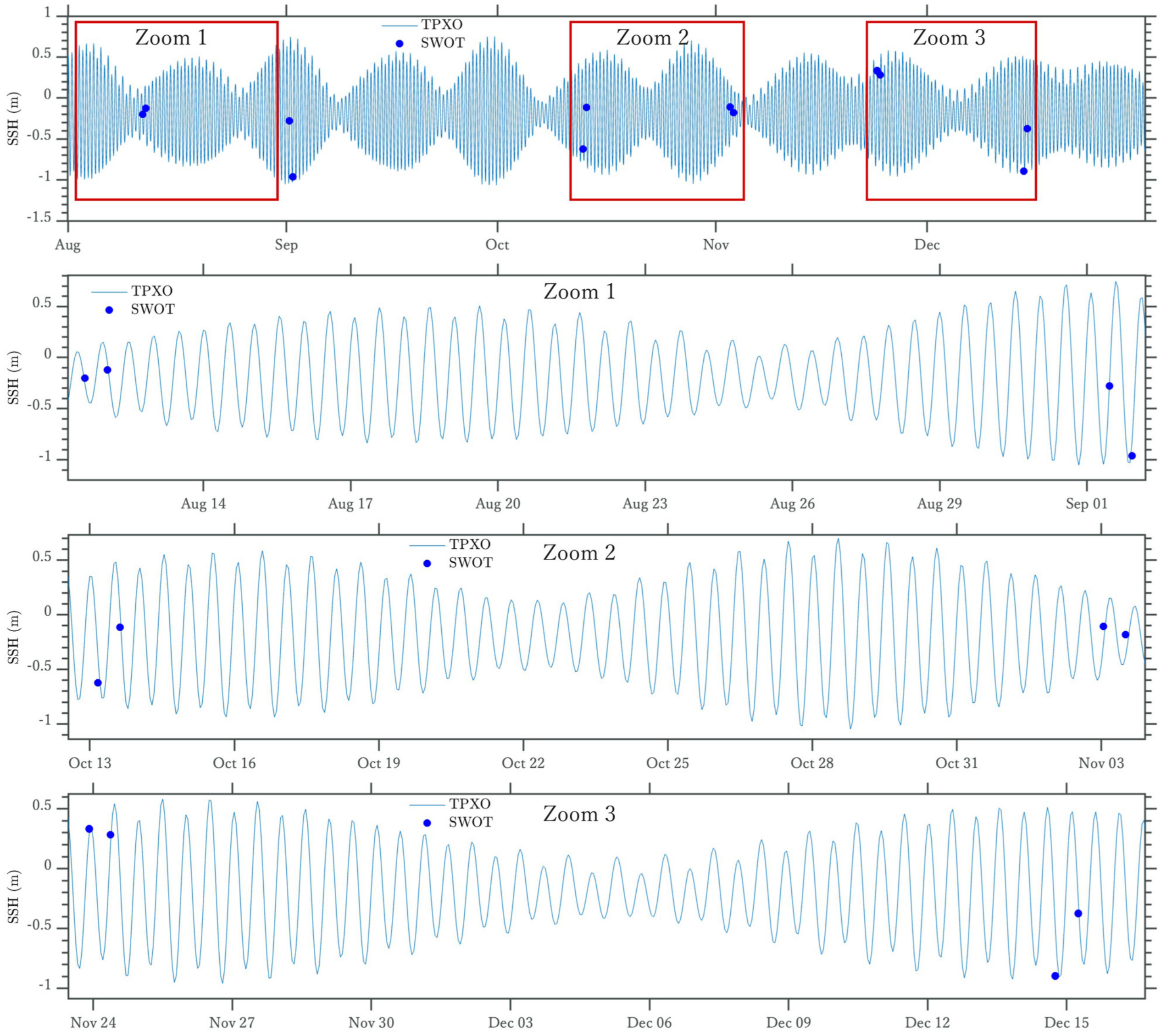

FIGURE 9
Comparison between TPXO-reconstructed sea surface height time series and SWOT sea surface heights for 16 passes along the model open boundary.

and could therefore transmit any bias into the domain. To assess the agreement, we reconstructed a TPXO tidal time series at the boundary and overlaid the collocated SWOT height points (Figure 9). For most passes, the SWOT points fell close to the TPXO curve, indicating good agreement, but the December 14 pass was a clear outlier, showing 0.42 m lower water level than the TPXO reconstruction. For other passes, differences between SWOT and TPXO ranged from 0.03 to 0.2 m. A scatter plot of all paired TPXO and SWOT values is shown in Figure 10. The two datasets were well correlated with $R^2 = 0.86$, although the RMSE was about 0.18 m.

To check whether part of the mismatch came from a timing offset rather than amplitude errors, we also ran a simple lag–correlation analysis between SWOT and the hourly TPXO time series at the boundary (Figure 11). We interpolated TPXO sea surface height to the SWOT pass times while scanning lags from −10 to +10 h in 1 min steps. The correlation decreased smoothly from about 0.6 at −10 h lags to a minimum of −0.95 in about −6 h and then increased smoothly to a maximum of 0.98 when TPXO was shifted by roughly +26 min relative to SWOT, and then declined again for larger positive lags. At this optimal lag the RMSE reached its minimum, about 0.11 m, compared with about 0.18 m at zero lag. This pattern indicates a small phase offset between TPXO and SWOT, with a modest residual mismatch that remains even after the timing is corrected. Both boundary phase and amplitude bias propagates into the domain primarily by shifting the timing and magnitude of the incoming tidal wave, which then affects the phase and amplitude of the water level inside the domain. In practical terms, a ~26 min boundary phase offset represents 4% of the M2 tidal harmonic constituent which is the dominant harmonic in the study area. This can translate into a noticeable timing shift in modeled interior water levels, with the strongest impact expected near the bay mouth and along the main tidal channels, and reduced influence farther inside the lagoon where friction and geometric constrictions damp and delay the signal. Another factor to consider is that TPXO supplies only the astronomical tide signal and cannot represent subtidal or supertidal

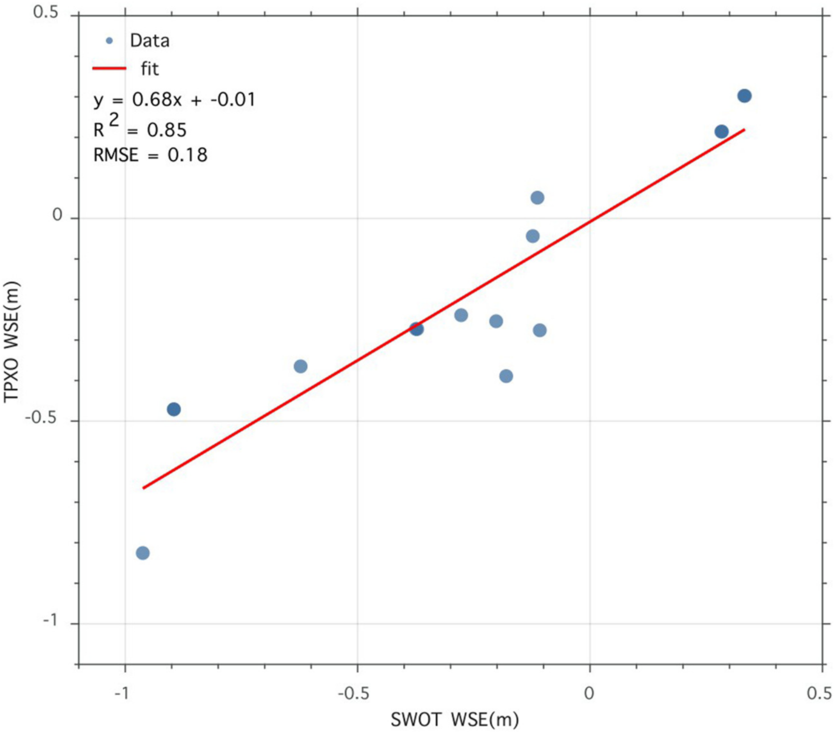

FIGURE 10
Scatter comparison between TPXO-reconstructed and SWOT observed sea surface heights at the model boundary for 16 satellite passes.

variations, baroclinic effects, or short lived meteorological surges unless those are adjusted at the boundary. A nested configuration could reduce boundary uncertainty by moving the open boundary farther offshore and allowing a larger scale model to represent both tidal propagation and wind driven subtidal variability before it reaches the local lagoon domain. In this setup, the regional model would be forced by a global tide solution (e.g., TPXO or FES) and atmospheric forcing, and the local model would inherit water levels and currents along its boundary from the regional solution. This approach can (i) diminish the sensitivity of the local solution to small boundary phase errors, (ii) better represent non-tidal variability at the boundary. We therefore view nesting as a practical next step to further improve model boundary accuracy.

4.3 Using SWOT for model calibration and validation

SWOT's unique advantage is its two-dimensional mapping of sea surface height, which provides dense, high resolution coverage across the land–ocean continuum, including estuaries and bays, that were previously data scarce. These data can improve calibration and validation of hydrodynamic models by filling in the spatial gaps between sparse tide gauges or *in situ* sensors. In particular, SWOT LR (Low-Rate) data delivers sea surface height on a 250 m grid with minimal smoothing (unsmoothed), which makes it well suited for model validation in shallow coastal areas. In our study we likewise used the Unsmoothed LR product (250 m resolution) to validate the model.

Recent field studies confirm that bias-corrected SWOT SSH (LR or HR) agrees closely with both gauges and model outputs in coastal systems. For example, Lichtman et al. (2025) evaluated SWOT LR in the hyper tidal Severn Estuary (United Kingdom) against water level gauges and found very low error: the bias corrected LR sea surface height had an RMSE of only ~0.14 m from gauges, with a nearly 1:1 linear relationship. In another study, Hart-Davis et al. (2024) used SWOT Cal/Val orbit data in the Bristol Channel (United Kingdom) and showed that the principal tidal amplitudes derived from SWOT matched gauge measurements to within ~0.018–0.03 m (amplitude errors of ~1.8–3.0 cm) and 1.75°–2.75° in phase. In a tropical estuary, Diouf et al. (2025) compared SWOT SSH (from high-rate (HR) pixel clouds) with a Delft3D hydrodynamic model in Senegal's Casamance Estuary: the SWOT data and model agreed very well in the main channel (correlation R ~ 0.90, RMSE $\lesssim$ 0.25 m) but showed larger scatter in narrow side channels (R ~ 0.42, RMSE up to ~ 0.34 m). Likewise, Arildsen et al. (2025) used unsmoothed high-rate SWOT SSH in the Bristol Channel and found that the SWOT data captured the Severn tidal bore and associated waves with high accuracy, even in intertidal zones; they emphasize that minimal smoothing is required to preserve these fine features.

These results imply that SWOT LR altimetry, once properly bias-corrected, provides reliable validation of coastal models. In line with these studies, our own model comparison with SWOT showed close agreement: the LR SSH differences between the model and SWOT are on the order of a few decimeters and the regression slope is near unity. In other words, the metrics we obtain (correlation and RMSE) are comparable to those reported above. Table 6, summarizes several recent SWOT calibration/validation studies, the environments they cover, the SWOT product used, and the key statistics (e.g., RMSE, correlation) that quantify model vs. agreement with gauge observations. All of these studies that range from open ocean and

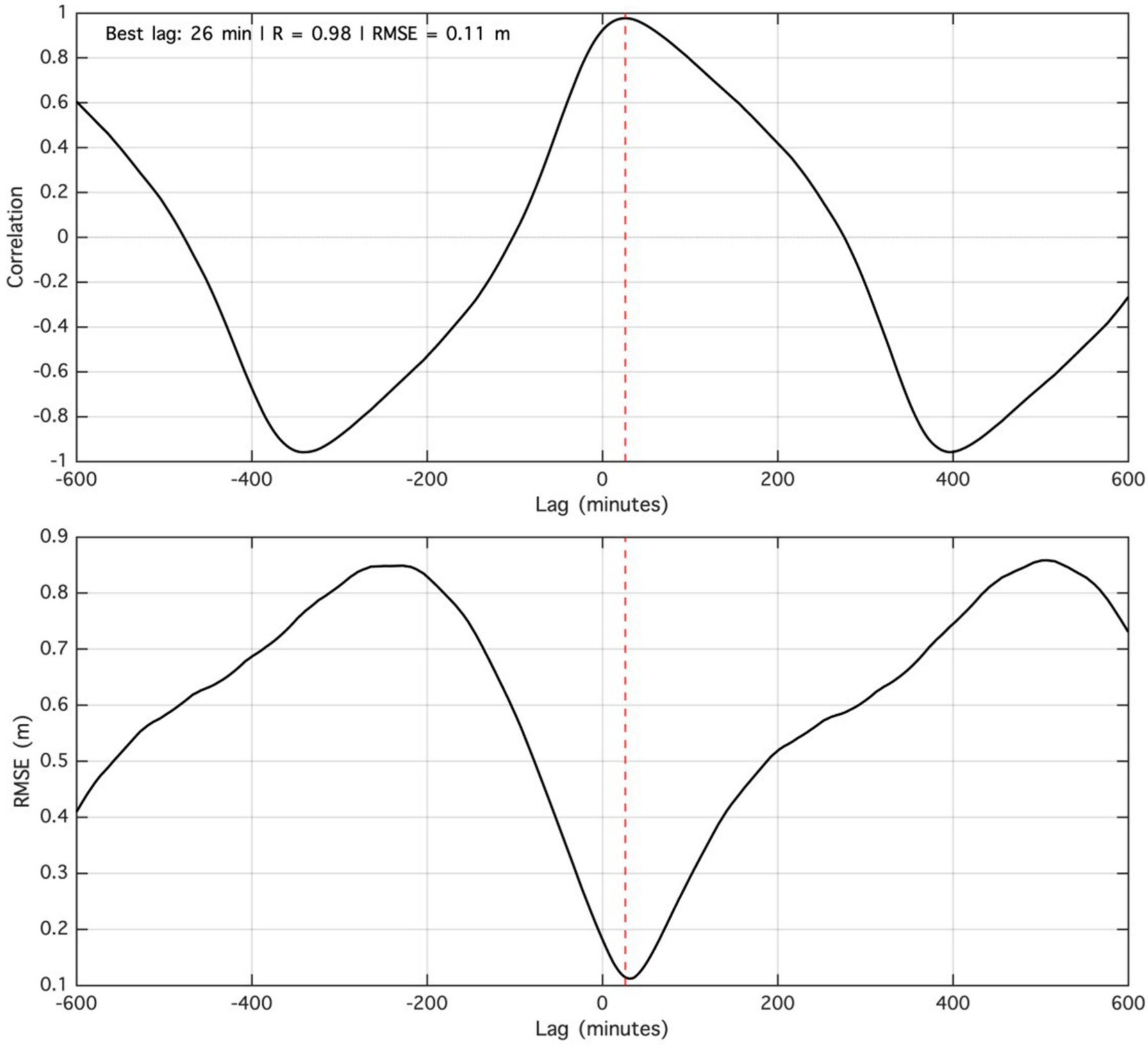

FIGURE 11
Cross-correlation analysis between SWOT and TPXO WSE time series at the offshore boundary. The upper panel shows the correlation coefficient as a function of temporal lag, and the lower panel shows the corresponding RMSE.

tidal basins to estuaries, inland aquatic lacustrine systems and rivers, demonstrate the value of SWOT's 2D sea surface height for improving and validating hydrodynamic simulations in the coastal zone.

5 Conclusion

This study shows that it is possible to build and validate a hydrodynamic model in a coastal lagoon without using any local field measurements. By combining satellite bathymetry from ICESat-2 and Sentinel-2 with a machine-learning approach, we were able to derive a spatially continuous bathymetry map for the Langebaan Lagoon. The XGBoost model optimized with Bayesian optimization captured the bathymetric variability from offshore depths to shallow lagoon channels, matching independent ATL24 data with an RMSE of 0.45 m and an R^2 of 0.97. Using tidal harmonics from TPXO for the boundary and atmospheric forcing from ERA5, the model reproduced the water surface patterns inside the lagoon. Validation using SWOT water level observations confirmed that the model results were consistent with satellite measurements across 16 passes, with an overall RMSE of 0.11 m and an R^2 of 0.61. SWOT's wide swath data allowed us to look beyond a single comparison point and instead evaluate spatial patterns across the entire lagoon. This greatly increases confidence in model performance, especially in places where *in situ* gauges are limited or do not exist. Although uncertainties remain, particularly from optical limitations in bathymetry and offsets between TPXO and SWOT at the boundary, the overall results demonstrate that remote sensing can support impressively accurate coastal hydrodynamic modeling in locations where direct measurements are not available. A key strength of this framework is that it integrates complementary remote sensing observations from passive optical sensors (Sentinel-2), spaceborne LiDAR (ICESat-2), and radar interferometry (SWOT), which reduces reliance on any single instrument and makes the approach more robust and transferrable. The approach presented

TABLE 6 **Summary of selected studies using SWOT to calibrate or validate hydrodynamic models or tidal predictions. Domains range from open coast and estuaries to large rivers, and products include low-rate (LR) and high-rate (HR) SWOT data. All report strong agreement between SWOT SSH and reference data, illustrating SWOT's utility for coastal model validation.**

Study (ref)	Domain	SWOT data	Compared to	Validation metrics
Lichtman et al. (2025)	Severn estuary, United Kingdom (hyper-tidal)	LR SSH (250 m, unsmoothed)	Tide gauges (water level)	RMSD $\approx$ 0.14 m; regression slope $\approx$ 0.99
Hart-Davis et al. (2024)	Bristol channel and great south bay	HR SSH (KaRIn, 1-day Cal/Val)	Tide gauges (tidal analysis)	Tide amplitude error $\approx$ 0.018–0.03 m; phase error $\approx$ 1.8°–2.8°
Diouf et al. (2025)	Casamance estuary, Senegal	HR SSH (pixel cloud)	Delft3D model	Main channel: $R \approx 0.90$, RMSE < 0.25 m; tributaries: $R \approx 0.42$, RMSE ≤ 0.34 m
Arildsen et al. (2025)	Severn river (bristol channel)	HR SSH (L2HR pixel cloud)	Two tide gauges	3.7 and 9.8 cm

here is therefore transferable to other data-scarce regions and offers a path toward cost-effective monitoring that does not depend on continuous field campaigns. With additional SWOT cycles and the release of more HR inland water level products, our method could be extended to narrower channels and more confined coastal systems, where finer spatial detail matters. Beyond water levels, the hydrodynamic model can be expanded into a coupled sediment/vegetation model, and future research can explore how satellite observations and global datasets can replace or supplement field inputs that such coupled models traditionally depend on.

Data availability statement

The original contributions presented in the study are included in the article/Supplementary Material, further inquiries can be directed to the corresponding author.

Author contributions

AP: Funding acquisition, Writing – review and editing, Validation, Software, Formal Analysis, Resources, Supervision, Methodology, Data curation, Writing – original draft, Conceptualization, Project administration, Investigation, Visualization. MS: Resources, Formal Analysis, Funding acquisition, Project administration, Methodology, Supervision, Investigation, Validation, Writing – review and editing, Conceptualization, Data curation. DJ: Formal Analysis, Validation, Writing – review and editing, Supervision, Funding acquisition. AnC: Supervision, Funding acquisition, Writing – review and editing, Resources, Validation. HD: Writing – review and editing. AlC: Writing – review and editing, Software.

Funding

The author(s) declared that financial support was received for this work and/or its publication. This research was carried out at the Jet Propulsion Laboratory, California Institute of Technology, under a contract with the National Aeronautics and Space Administration (NASA 80NM0018D0004). Authors MS, AC and AP were supported by the Surface Water and Ocean Topography Science Team (NNH23ZDA001N-SWOTST) and AP, AnC, DJ by the BIOSCAPE (NNH21ZDA001N-BIODIV) Programs.

Conflict of interest

The author(s) declared that this work was conducted in the absence of any commercial or financial relationships that could be construed as a potential conflict of interest.

Generative AI statement

The author(s) declared that generative AI was not used in the creation of this manuscript.

Publisher's note

Supplementary material

The Supplementary Material for this article can be found online at: https://www.frontiersin.org/articles/10.3389/frsen.2026.1751006/full#supplementary-material

References

Arildsen, R., Andersen, O., Nilsson, B., and Ludwigsen, C. (2025). Tidal bore revealed by swot: a case study from the Severn River. *Sci. Rep.* 15, 22776. doi:10.1038/s41598-025-99597-2

Ashphaq, M., Srivastava, P. K., and Mitra, D. (2021). Review of near-shore satellite derived bathymetry: classification and account of five decades of coastal bathymetry research. *J. Ocean Eng. Sci.* 6, 340–359. doi:10.1016/j.joes.2021.02.006

Babbel, B. J., Parrish, C. E., and Magruder, L. A. (2021). Icesat-2 elevation retrievals in support of satellite-derived bathymetry for global science applications. *Geophys. Research Letters* 48, e2020GL090629. doi:10.1029/2020GL090629

Badcock, R. M., and Barnes, R. (1981). Coastal lagoons. the natural history of a neglected habitat. *J. Ecol.* 69, 1061. doi:10.2307/2259652

Balasubramanian, S. V., Pahlevan, N., Smith, B., Binding, C., Schalles, J., Loisel, H., et al. (2020). Robust algorithm for estimating total suspended solids (tss) in inland and nearshore coastal waters. *Remote Sens. Environ.* 246, 111768. doi:10.1016/j.rse.2020.111768

Båmstedt, U., and Brugel, S. (2017). A cost-precision model for marine environmental monitoring, based on time-integrated averages. *Environ. Monit. Assess.* 189, 354. doi:10.1007/s10661-017-6064-6

[Dataset] Brush, M. J., and Harris, L. A. (2010). “Introduction to the special issue of ecological modelling:advances in modeling estuarine and coastal ecosystems,” in *Approaches, validation, and applications*.

Caballero, I., and Stumpf, R. P. (2020). Towards routine mapping of shallow bathymetry in environments with variable turbidity: contribution of sentinel-2a/b satellites mission. *Remote Sens.* 12, 451. doi:10.3390/rs12030451

Caballero, I., Fernández, R., Escalante, O. M., Mamán, L., and Navarro, G. (2020). New capabilities of sentinel-2a/b satellites combined with *in situ* data for monitoring small harmful algal blooms in complex coastal waters. *Sci. Reports* 10, 8743. doi:10.1038/s41598-020-65600-1

Casal, G., Monteys, X., Hedley, J., Harris, P., Cahalane, C., and McCarthy, T. (2019). Assessment of empirical algorithms for bathymetry extraction using sentinel-2 data. *Int. J. Remote Sens.* 40, 2855–2879. doi:10.1080/01431161.2018.1533660

Cea, L., and French, J. (2012). Bathymetric error estimation for the calibration and validation of estuarine hydrodynamic models. *Estuar. Coast. Shelf Sci.* 100, 124–132. doi:10.1016/j.ecss.2012.01.004

Chénier, R., Faucher, M.-A., and Ahola, R. (2018). Satellite-derived bathymetry for improving canadian hydrographic service charts. *ISPRS Int. J. Geo-Information* 7, 306. doi:10.3390/ijgi7080306

Chézy, A. (1775). *Note sur la formule de la vitesse de l’eau dans les canaux. Unpublished manuscript*. Paris: École Nationale des Ponts et Chaussées.

Christensen, A. L. (2025). *Swot_coasts*. GitHub repository. Available online at: https://github.com/achri19/SWOT_Coasts (Accessed November 20, 2025).

Ciancia, E., Campanelli, A., Lacava, T., Palombo, A., Pascucci, S., Pergola, N., et al. (2020). Modeling and multi-temporal characterization of total suspended matter by the combined use of sentinel 2-msi and landsat 8-oli data: the pertusillo lake case study (italy). *Remote Sens.* 12, 2147. doi:10.3390/rs12132147

Corcoran, F., Parrish, C. E., Magruder, L. A., and Swinski, J. (2024). A scalable, cloud-based workflow for spectrally-attributed icesat-2 bathymetry with application to benthic habitat mapping using deep learning. *Earth Space Sci.* 11, e2024EA003735. doi:10.1029/2024ea003735

Deltares (2021). *Delft3D FM Suite; D-flow manual*. Technical report, deltares. Version as of 2021.

Diouf, A., Salameh, E., Sakho, I., Sow, B. A., Deloffre, J., López Solano, C., et al. (2025). Use of swot data for hydrodynamic modelling in a tropical microtidal estuarine system: the case of casamance (senegal). *Remote Sens.* 17, 3252. doi:10.3390/rs17183252

Du Toit, L., Henrico, I., Bezuidenhout, J., and Mtshawu, B. (2022). Analysing the changes in the bathymetry of Saldanha bay between the years 1977 and 2021. *South Afr. J. Geomatics* 11, 325–339. doi:10.4314/sajg.v11i2.11

Dullaart, J. C., Muis, S., Bloemendaal, N., and Aerts, J. C. (2020). Advancing global storm surge modelling using the new era5 climate reanalysis. *Clim. Dyn.* 54, 1007–1021. doi:10.1007/s00382-019-05044-0

Egbert, G. D., and Erofeeva, S. Y. (2002). Efficient inverse modeling of barotropic ocean tides. *J. Atmos. Ocean. Technology* 19, 183–204. doi:10.1175/1520-0426(2002)019<0183:eimobo>2.0.co;2

Essel, B., Gyesi, J. K., Addo, R. K., Galley, W., and MacCarthy, G. (2019). The tale of a disappearing lagoon: a habitat mapping and ecological assessment of fosu lagoon, Ghana. *Int. Journal Ecology* 2019, 6931329. doi:10.1155/2019/6931329

Forfinski-Sarkozi, N. A., and Parrish, C. E. (2016). Analysis of mabel bathymetry in keweenaw bay and implications for icesat-2 atlas. *Remote Sens.* 8, 772. doi:10.3390/rs8090772

Ganju, N. K., Brush, M. J., Rashleigh, B., Aretxabaleta, A. L., Del Barrio, P., Grear, J. S., et al. (2016). Progress and challenges in coupled hydrodynamic-ecological estuarine modeling. *Estuaries Coasts* 39, 311–332. doi:10.1007/s12237-015-0011-y

Gregg, D. E., Penna, N. T., Jones, C., and Maqueda, M. A. M. (2024). Accuracy assessment of recent global ocean tide models in coastal waters of the european north west shelf. *Ocean. Model.* 192, 102448. doi:10.1016/j.ocemod.2024.102448

Hanekom, N., Randall, R., Nel, P., and Kruger, N. (2009). *West coast national park state of knowledge report*. South African National Parks, 1–65.

Harmel, T., Chami, M., Tormos, T., Reynaud, N., and Danis, P.-A. (2018). Sunglint correction of the multi-spectral instrument (msi)-sentinel-2 imagery over inland and sea waters from swir bands. *Remote Sens. Environ.* 204, 308–321. doi:10.1016/j.rse.2017.10.022

Hart-Davis, M., Andersen, O., Ray, R., Zaron, E., Schwatke, C., Arildsen, R., et al. (2024). Tides in complex coastal regions: early case studies from wide-swath swot measurements. *Geophys. Res. Lett.* 51, e2024GL109983. doi:10.1029/2024gl109983

Henrico, I., and Bezuidenhout, J. (2020). Determining the change in the bathymetry of saldanha bay due to the harbour construction in the seventies. *South Afr. J. Geomatics* 9, 236–249. doi:10.4314/sajg.v9i2.16

Hersbach, H., Bell, B., Berrisford, P., Hirahara, S., Horányi, A., Muñoz-Sabater, J., et al. (2020). The era5 global reanalysis. *Q. Journal Royal Meteorological Society* 146, 1999–2049. doi:10.1002/qj.3803

Jasinski, M. F., Stoll, J. D., Cook, W. B., Ondrusek, M., Stengel, E., and Brunt, K. (2016). Inland and near-shore water profiles derived from the high-altitude multiple altimeter beam experimental lidar (mabel). *J. Coast. Res.* 76, 44–55. doi:10.2112/si76-005

Jung, J., Parrish, C. E., Magruder, L. A., Herrmann, J., Yoo, S., and Perry, J. S. (2025). Icesat-2 bathymetry algorithms: a review of the current state-of-the-art and future outlook. *ISPRS J. Photogrammetry Remote Sens.* 223, 413–439. doi:10.1016/j.isprsjprs.2025.03.016

Kirwan, M. L., and Megonigal, J. P. (2013). Tidal wetland stability in the face of human impacts and sea-level rise. *Nature* 504, 53–60. doi:10.1038/nature12856

Kirwan, M. L., and Mudd, S. M. (2012). Response of salt-marsh carbon accumulation to climate change. *Nature* 489, 550–553. doi:10.1038/nature11440

Krug, M. (1999). Circulation through the mouth of langebaan lagoon and implications.

Large, W., and Pond, S. (1981). Open ocean momentum flux measurements in moderate to strong winds. *J. Physical Oceanography* 11, 324–336. doi:10.1175/1520-0485(1981)011<0324:oomfmi>2.0.co;2

Le, Y., Sun, X., Chen, Y., Zhang, D., Wu, L., Liu, H., et al. (2024). High-accuracy shallow-water bathymetric method including reliability evaluation based on sentinel-2 time-series images and icesat-2 data. *Front. Mar. Sci.* 11, 1470859. doi:10.3389/fmars.2024.1470859

Lichtman, I., Bell, P., Gommenginger, C., Banks, C., Calafat, F., Brown, J., et al. (2025). Evaluating water levels from the surface water and ocean topography (swot) mission in a hyper-tidal coastal and estuarine environment. *Earth Space Sci.* 12, e2024EA004104. doi:10.1029/2024ea004104

Miththapala, S. (2013). *Lagoons and estuaries*, 4. IUCN.

Mohseni, F., Saba, F., Mirmazloumi, S. M., Amani, M., Mokhtarzade, M., Jamali, S., et al. (2022). Ocean water quality monitoring using remote sensing techniques: a review. *Mar. Environmental Research* 180, 105701. doi:10.1016/j.marenvres.2022.105701

Morrow, R., Fu, L.-L., Ardhuin, F., Benkiran, M., Chapron, B., Cosme, E., et al. (2019). Global observations of fine-scale ocean surface topography with the surface water and ocean topography (swot) mission. *Front. Mar. Sci.* 6, 232. doi:10.3389/fmars.2019.00232

Najar, M. A., Benshila, R., Bennioui, Y. E., Thoumyre, G., Almar, R., Bergsma, E. W., et al. (2022). Coastal bathymetry estimation from sentinel-2 satellite imagery: comparing deep learning and physics-based approaches. *Remote Sens.* 14, 1196. doi:10.3390/rs14051196

NASA/PO.DAAC (2025). *Swot data user handbook*. Available online at: https://podaac.github.io/tutorials/quarto_text/SWOT.html (Accessed October 10, 2025).

NOAA National Ocean Service (2025). *VDatum Interpolat. Transformation Grid Format (GTX Files)*. Available online at: https://vdatum.noaa.gov/docs/gtx_info.html (Accessed September 17, 2025).

Pacheco, A., Horta, J., Loureiro, C., and Ferreira, Ó. (2015). Retrieval of nearshore bathymetry from landsat 8 images: a tool for coastal monitoring in shallow waters. *Remote Sens. Environ.* 159, 102–116. doi:10.1016/j.rse.2014.12.004

Page, B. P., Olmanson, L. G., and Mishra, D. R. (2019). A harmonized image processing workflow using sentinel-2/msi and landsat-8/oli for mapping water clarity in optically variable lake systems. *Remote Sens. Environ.* 231, 111284. doi:10.1016/j.rse.2019.111284

Parrish, C. E., Magruder, L. A., Neuenschwander, A. L., Forfinski-Sarkozi, N., Alonzo, M., and Jasinski, M. (2019). Validation of icesat-2 atlas bathymetry and analysis of atlas’s bathymetric mapping performance. *Remote Sensing* 11, 1634. doi:10.3390/rs11141634

Parrish, C. E., Magruder, L. A., Perry, J., Holwill, M., Swinski, J., and Kief, K. (2025). Analysis and accuracy assessment of a new global nearshore icesat-2 bathymetric data product. *Earth Space Sci.* 12, e2025EA004391. doi:10.1029/2025ea004391

Payandeh, A., Justic, D., Mariotti, G., Huang, H., and Sorourian, S. (2019). Subtidal water level and current variability in a bar-built estuary during cold front season: barataria bay, gulf of Mexico. *J. Geophys. Res. Oceans* 124, 7226–7246. doi:10.1029/2019jc015081

Payandeh, A. R., Justic, D., Mariotti, G., Huang, H., Valentine, K., and Walker, N. D. (2021). Suspended sediment dynamics in a deltaic estuary controlled by subtidal motion and offshore river plumes. *Estuar. Coast. Shelf Sci.* 250, 107137. doi:10.1016/j.ecss.2020.107137

Payandeh, A. R., Justic, D., Huang, H., Mariotti, G., and Hagen, S. C. (2022). Tidal change in response to the relative sea level rise and marsh accretion in a tidally choked estuary. *Cont. Shelf Res.* 234, 104642. doi:10.1016/j.csr.2021.104642

Payandeh, A., Simard, M., and Jones, C. (2025). *Delta-x: Delft3d fm, extended domain hydrodynamic model.* usa: ornl daac, oak ridge, tennessee.

Schuerch, M., Spencer, T., Temmerman, S., Kirwan, M. L., Wolff, C., Lincke, D., et al. (2018). Future response of global coastal wetlands to sea-level rise. *Nature* 561, 231–234. doi:10.1038/s41586-018-0476-5

Simard, M., Jones, C. E., Twilley, R. R., Castañeda-Moya, E., Fagherazzi, S., Fichot, C. G., et al. (2026). Delta-x: an airborne remote sensing framework to calibrate hydrodynamic and ecogeomorphic processes responsible for land building in coastal deltas. *Remote Sens. Environ.* 334, 115201. doi:10.1016/j.rse.2025.115201

Sorourian, S., Huang, H., Li, C., Justic, D., and Payandeh, A. R. (2020). Wave dynamics near barataria Bay tidal inlets during spring–summer time. *Ocean. Model.* 147, 101553. doi:10.1016/j.ocemod.2019.101553

Spencer, T., Schuerch, M., Nicholls, R. J., Hinkel, J., Lincke, D., Vafeidis, A., et al. (2016). Global coastal wetland change under sea-level rise and related stresses: the diva wetland change model. *Glob. Planet. Change* 139, 15–30. doi:10.1016/j.gloplacha.2015.12.018

Stammer, D., Ray, R. D., Andersen, O. B., Arbic, B. K., Bosch, W., Carrere, L., et al. (2014). Accuracy assessment of global barotropic ocean tide models. *Rev. Geophysics* 52, 243–282. doi:10.1002/2014rg000450

Traganos, D., Poursanidis, D., Aggarwal, B., Chrysoulakis, N., and Reinartz, P. (2018). Estimating satellite-derived bathymetry (sdb) with the google earth engine and sentinel-2. *Remote Sens.* 10, 859. doi:10.3390/rs10060859

Van Niekerk, L., Lamberth, S. J., James, N. C., Taljaard, S., Adams, J. B., Theron, A. K., et al. (2022). The vulnerability of south African estuaries to climate change: a review and synthesis. *Diversity* 14, 697. doi:10.3390/d14090697

Vanhellemont, Q. (2019). Adaptation of the dark spectrum fitting atmospheric correction for aquatic applications of the landsat and sentinel-2 archives. *Remote Sens. Environ.* 225, 175–192. doi:10.1016/j.rse.2019.03.010

Vanhellemont, Q. (2020). Sensitivity analysis of the dark spectrum fitting atmospheric correction for metre-and decametre-scale satellite imagery using autonomous hyperspectral radiometry. *Opt. Express* 28, 29948–29965. doi:10.1364/OE.397456

Vanhellemont, Q., and Ruddick, K. (2016). "Acolite for sentinel-2: aquatic applications of msi imagery," in *Proceedings of the 2016 ESA living planet symposium*, 9. Prague, Czech Republic.

Vanhellemont, Q., and Ruddick, K. (2018). Atmospheric correction of metre-scale optical satellite data for inland and coastal water applications. *Remote Sensing Environment* 216, 586–597. doi:10.1016/j.rse.2018.07.015

Vargas-Yáñez, M., Moreno, C. A., Fernández, E. B., Aguado, S. S., Martínez, M. C. G., Zounon, Y., et al. (2025). A study on the suitability of *in situ* ocean observing systems through fixed stations and periodic campaigns: the importance of sampling frequency and spatial coverage. *Water* 17, 620. doi:10.3390/w17050620

Wang, D., Ma, R., Xue, K., and Loiselle, S. A. (2019). The assessment of landsat-8 oli atmospheric correction algorithms for inland waters. *Remote Sens.* 11, 169. doi:10.3390/rs11020169

Wang, J., Lee, Z., Wang, D., Shang, S., Wei, J., and Gilerson, A. (2021). Atmospheric correction over coastal waters with aerosol properties constrained by multi-pixel observations. *Remote Sens. Environ.* 265, 112633. doi:10.1016/j.rse.2021.112633

Wei, J., Wang, M., Lee, Z., Briceño, H. O., Yu, X., Jiang, L., et al. (2020). Shallow water bathymetry with multi-spectral satellite ocean color sensors: leveraging temporal variation in image data. *Remote Sens. Environ.* 250, 112035. doi:10.1016/j.rse.2020.112035

Wei, C., Xiao, Y., Fu, D., and Zhou, T. (2024). Impact of turbidity on satellite-derived bathymetry: comparative analysis across seven ports in the South China sea. *Remote Sens.* 16, 4349. doi:10.3390/rs16234349

Whitfield, A., Bate, G., Adams, J., Cowley, P., Froneman, P., Gama, P., et al. (2012). A review of the ecology and management of temporarily open/closed estuaries in South Africa, with particular emphasis on river flow and mouth state as primary drivers of these systems. *Afr. J. Mar. Sci.* 34, 163–180. doi:10.2989/1814232x.2012.675041

Williams, J. J., and Esteves, L. S. (2017). Guidance on setup, calibration, and validation of hydrodynamic, wave, and sediment models for shelf seas and estuaries. *Adv. Civil Engineering* 2017, 5251902–5251925. doi:10.1155/2017/5251902

Xu, N., Wang, L., Zhang, H.-S., Tang, S., Mo, F., and Ma, X. (2023). Machine learning based estimation of coastal bathymetry from icesat-2 and sentinel-2 data. *IEEE J. Sel. Top. Appl. Earth Observations Remote Sens.* 17, 1748–1755. doi:10.1109/jstars.2023.3326238

Yang, Z., Shao, W., Ding, Y., Shi, J., and Ji, Q. (2020). Wave simulation by the swan model and fvcom considering the sea-water level around the zhoushan islands. *J. Mar. Sci. Eng.* 8, 783. doi:10.3390/jmse8100783

Zaron, E. D., and Elipot, S. (2020). An assessment of global ocean barotropic tide models using geodetic mission altimetry and surface drifters. *J. Phys. Oceanogr.* 51, 63–82. doi:10.1175/jpo-d-20-0089.1

Zundel, A. (2000). *Surface-water modeling system reference manual.* Brigham Young University, Environmental Modeling Research Laboratory, 79.